HOKKAIDO UNIVERSITY

Title	Nitrogen-doped porous carbon as-mediated by a facile solution combustion synthesis for supercapacitor and oxygen reduction electrocatalyst
Author(s)	Zhu, Chunyu; Takata, Manami; Aoki, Yoshitaka et al.
Citation	Chemical engineering journal, 350, 278-289 https://doi.org/10.1016/j.cej.2018.06.001
Issue Date	2018-10-15
Doc URL	https://hdl.handle.net/2115/79534
Rights	© 2018. This manuscript version is made available under the CC-BY-NC-ND 4.0 license https://creativecommons.org/licenses/by-nc-nd/4.0/
Rights(URL)	https://creativecommons.org/licenses/by-nc-nd/4.0/
Type	journal article
File Information	manuscript.pdf

Hokkaido University Collection of Scholarly and Academic Papers : HUSCAP

Nitrogen-doped porous carbon as-mediated by a facile solution combustion synthesis for supercapacitor and oxygen reduction electrocatalyst

Chunyu ZHU[a,b]*, Manami TAKATA[a], Yoshitaka AOKI [a,b], Hiroki HABAZAKI [a,b]

[a] Graduate School of Chemical Sciences and Engineering, Hokkaido University, Sapporo, Hokkaido 060-8628, Japan

[b] Division of Applied Chemistry, Faculty of Engineering, Hokkaido University, Sapporo, Hokkaido 060-8628, Japan

Corresponding author: chunyu6zhu@eng.hokudai.ac.jp

Abstract

Porous carbon has attracted great interest because of its distinctive structure and superior properties for designing electrochemical energy storage devices. In this work, we report a novel and facile method to fabricate nitrogen-doped porous carbon (NPC) with designed hierarchical multi-porous structure. The NPC is prepared using a facile and scalable MgO template method as-mediated by a magnesium nitrate-glycine solution combustion synthesis (SCS), in which the preparation conditions of calcination temperature and glycine-nitrate ratio are carefully studied. The NPC shows a high specific surface area up to 1958 m^2 g^{-1} and contains hierarchical multi-pores of interconnected macro-, meso- and micro-pores. When applied as ORR electrocatalyst, the NPC-n2-1000 sample shows the highest activity, good durability and high tolerance against methanol, which is among the best reported carbon-base catalysts. The NPC samples also shows great potential as the active electrode material for supercapacitors. NPC-n2-900 sample exhibits a high specific capacitance of 232 F g^{-1} at 1 A g^{-1} in 6 M KOH electrolyte, a superior rate capability (205 F g^{-1} at 10 A g^{-1}) and a good cycling performance. The present work demonstrates that the combination of glycine-nitrate SCS and template introduction in one-step can turn the carbohydrate fuel to advanced porous carbon with prospective applications in high-performance energy storage devices.

Keywords: supercapacitor, oxygen reduction reaction, porous carbon, solution combustion synthesis, MgO template

1. Introduction

Carbon is one of the most abundant and useful elements in nature, for example, the whole organic chemistry is built on carbon. Carbon materials also play an increasingly important role in electrochemical energy storage and conversion devices, including batteries, fuel cells and electrochemical supercapacitors, in which carbon is used as the electrode active material or as the conductive additive & support.[1-8] Recently, porous carbon materials have received significant attention in various electrochemical electrodes because of their attractive properties, such as ready abundance, chemical and thermal stability, easy processability, wide availability, high specific surface area (SSA), and tunable pore size.[1, 3, 5, 9] The high SSA porous carbons are the best commercially available electrode material for electrochemical supercapacitor, also known as electrical double layer capacitor (EDLC). [3, 5, 10-17] Porous carbon materials are also promising electrocatalysts or catalyst support to facilitate the oxygen reduction reaction, which is the core cathodic reaction in fuel cells and metal air batteries.[18-21] To achieve a high-performance in EDLC or ORR electrocatalyst, the active carbon materials with well-defined pore structure and heteroatom-doping (N, S, P et al.) have been regarded as the most effective strategies. In particular, a well-developed hierarchical pore structure, which has a three-dimensionally multi-porous architecture with interconnected micro-, meso- and macropores, is very promising since that the electrochemical reactions mainly occur at the electrode and electrolyte interfaces. In such a hierarchical structure, the abundant micro- and mesopores can provide large accessible surface areas and abundant active sites for the electrochemical processes, while the interconnected meso- and macropores can facilitate the fast ion transport by supplying electrolyte-buffering reservoirs and shortened

ion-transport pathways.[10, 15, 22-26] On the other hand, heteroatom-doping, especially N-doping, is another attractive method to improve the EDLC and ORR electrocatalytic performance.[27-34] Heteroatomic N-doping to the carbon materials can substantially improve the supercapacitive performance since the heteroatoms are electrochemically active which can provide extra pseudocapacitance due to the faradaic interactions between electrolyte ions and carbon surface, at the same time, the surface wettability and electronic conductivity of carbon are also enhanced by introducing heteroatoms.[28, 29, 32, 35] As for the carbon-based ORR electrocatalysts, the incorporation of electronegative N atoms induces a charge delocalization in the sp^2-hybridized carbon framework which facilitates oxygen adsorption and reduction, leading to the significant enhancement in ORR performance.[27, 30, 36-39]

In this circumstance, the development of a simple, inexpensive and effective synthetic method for preparing porous carbon with well-developed hierarchical porosity and simultaneous N-doping is of great interest for applications both for EDLC and ORR electrocatalysts. Therefore, in this work, we present a novel, facile and scalable synthesis strategy to fabricate a nitrogen-rich porous carbon (NPC), which contains hierarchical multi-pores of interconnected macro-, meso- and micro-pores. The NPC was prepared by a facile MgO template method. The MgO@C precursors were fabricated via a solution combustion synthesis (SCS) of the corresponding metal nitrate and glycine mixture, followed by a high-temperature heat treatment. After the removal of the template with acid etching, the nitrogen-doped carbon sample exhibited a highly porous structure consisting hierarchical multi-pores. Macro-pores and large mesopores were formed during the SCS process, whereas additional meso-pores and micro-pores were created by high-temperature heat treatment and MgO-template removal. The

potential of the obtained NPC as EDLC electrode and ORR electrocatalyst was explored and the sample showed superior electrochemical performance.

2. Experimental section

Synthesis of NPC: In the experiment, first, magnesium nitrates hexahydrate ($Mg(NO_3)_2 \cdot 6H_2O$, 10 mmol) and glycine (NH_2CH_2COOH, 20, 25, and 30 mmol, respectively, making the molar ratio of glycine to nitrate n = 2, 2.5 and 3) were dissolved in 2 mL distilled water to form homogenous solutions; then the solutions were evaporated on a hot plate with magnetic stirring to form dried gels. The obtained gels were first heated to 500 ^oC at a temperature ramp of 10 $^oC\ min^{-1}$ under Ar flow to preliminarily decompose the nitrate and organic material. This step is the solution combustion synthesis. Subsequently, the pyrolyzed samples were pulverized using a mortar and pestle. The samples were then heated to 800-1100 ^oC at a temperature ramp of 10 $^oC\ min^{-1}$ and kept at this temperature for 2 h under Ar flow. Finally, the samples were leached with HCl solution, filtered, washed with distilled water/ethanol for several times, and dried to obtain porous carbon materials.

The samples were named based on the molar ratio (n) of glycine to nitrate and heat treatment teperature, such as NPC-n2-900, NPC-n2.5-900, NPC-n3-900 and so on.

Material characterization: The samples were characterized by X-ray diffraction (XRD, Rigaku Miniflex, CuKα), transmission electron microscopy (TEM, 200 kV, JEM-2010F and JEM-2010), and scanning electron microscopy (SEM, JEOL JSM-7400F and ZEISS Sigma 500) for their crystalline structure and morphology observation. Surface functional groups and bonding characterization of the samples

were performed on X-ray photoelectron spectroscopy (XPS, JEOL, JPS-9200) system using Mg-Kα X-ray source. Raman spectra of the samples were acquired using a RENISHAW Raman spectrometer using an excitation wavelength of 532 nm. The pyrolysis behavior of the gel precursors was confirmed by a thermogravimetric (TG) analyzer combied with a differential thermal analyzer (DTA) (STA 2500 Regulus). TG was also used to determine the carbon contents in the calcined MgO@C precursors by combusting the samples under air flow. The pore volumes, SSA and pore size distributions of the samples were characterized by nitrogen adsorption using a Microtrac-BEL (BELSORP-mini) surface area analyzer. The total pore volumes ($V_{0.99}$ and $V_{0.95}$) were determined from the amount of nitrogen adsorbed at the relative pressure P/P_0 of 0.99 and 0.95, corresponding to pores with diameters up to around 200 and 40 nm, respectively. The SSA were calculated by both Brunauer-Emmett-Teller (BET) and t-plot methods. The pressure range of 0.05 to 0.25 is used for BET SSA calculation. The t-plot analysis deduced the total surface area (a_{total}), external surface area (a_{ex}) and micropore volume (V_{micro}). Based on this, the micropore surface area (a_{micro}) was determined by a_{total}-a_{ex}, and the mesopore volume (V_{meso}) was calculated by $V_{0.95}$-V_{micro}. Here $V_{0.95}$ was used as the sum of meso- and micropore to avoid the over estimation of mesopore volume. The pore size distributions were estimated by both Barrette-Joynere-Halenda (BJH) and non localized density functional theory (NLDFT) methods. The absorption isotherm is used for the BJH analysis.

Electrochemical measurement for ORR electrocatalytic activity: The ORR electrocatalytic performance was measured in a typical three-electrode system [40, 41] on a Princeton electrochemical analyzer, in which a platinum plate, a saturated Ag/AgCl electrode, and a rotating disk electrode (RDE) were used as the counter, reference and

working electrode, respectively. 2.0 mg of catalyst materials or a commercial carbon black (KETJEN BLACK (KB), EC600JD) was dispersed in 0.4 mL ethanol with the addition of 20 μL 5% Nafion solution, which was ultrasonic agitated for at least 30 minutes, to make the catalyst ink. The working electrode equipped with a polished glassy carbon, with a diameter of 5 mm, was cast with 8 μL catalyst ink and dried in air. Before every measurement, the 0.1 M KOH electrolyte solution was saturated with Ar or O_2 gas for at least 30 min. The linear sweep voltammetry (LSV) measurement for ORR was carried out at a scan rate of 5 mV s^{-1}, which was performed at RDE rotation rate ranging from 400 to 1600 rpm. Cyclic voltammetry (CV) was conducted in both Ar and O_2 saturated electrolyte at a scan rate of 50 mV s^{-1}. The measured potentials were converted to the reversible hydrogen electrode (RHE) via the Nernst equation:

$$E_{RHE} = E_{Ag/AgCl} + 0.059pH + 0.197\ V \qquad (1)$$

The electron transfer number (n) per oxygen molecule involved was calculated by using Koutecky–Levich (K-L) equations:

$$\frac{1}{j} = \frac{1}{j_L} + \frac{1}{j_K} = \frac{1}{B\omega^{1/2}} + \frac{1}{j_K} \qquad (2)$$

$$B = 0.62nFC_0{D_0}^{2/3}v^{-1/6} \qquad (3)$$

$$j_K = nFkC_0 \qquad (4)$$

in which j is the measured current density; j_L and j_K are the diffusion-limiting and kinetic current densities (mA cm^{-2}), respectively. n is the overall number of electrons gained per O_2, C_0 is the bulk concentration of O_2 (1.2×10^{-6} mol cm^{-3}), F is the Faraday constant (F = 96485 C mol^{-1} = 96485000 mA s mol^{-1}), D_0 is the diffusion coefficient of O_2 in 0.1 M KOH electrolyte (1.9×10^{-5} cm^2 s^{-1}), v is the kinetic viscosity of the electrolyte (0.01 cm^2 s^{-1}), ω is the angular velocity of the disk (rad/s) ($\omega = 2\pi N$, N is the linear rotation speed at rotation per second) and k is the electron transfer rate constant.

Electrochemical measurement for supercapacitor: A Swagelok-type symmetric two-electrode configuration was used for the supercapacitor electrochemical measurement. The working electrode was prepared by mixing the NPC, acetylene black conductive carbon, and polytetrafluroethylene (PTFE)-coated teflonized acetylene black (TAB-2®) binder with a weight ratio of 80:10:10 in ethanol to form a dough-like paste, which was pressed onto the nickel foam current collector with a diameter of 9 mm. The mass load of electrode material is about 3.5 mg cm^{-2}. The performance for the supercapacitors was measured within a potential range from 0 to 1 V in a 6 mol L^{-1} KOH aqueous electrolyte. Cyclic voltammetry (CV) was carried out on a potentiostat/galvanostat electrochemistry workstation (Princeton). The galvanostatic charge and discharge measurements were conducted in a battery tester (Hokudo Denko) at a constant temperature of 25 ºC. As a comparison, the commercial carbon black (KETJEN BLACK, EC600JD), which has a high SSA, is also used for the supercapacitor measurement.

The specific capacitance of a single carbon electrode was calculated based on the following equation:

$$C = \frac{2I\Delta t}{m\Delta V} \qquad (5)$$

where C (F g^{-1}) is the specific capacitance, I (A g^{-1}) is current density, Δt (s) is discharge time, m (g) is the mass of a single electrode, and ΔV (V) is the potential window during the discharge process (excluding the IR drop), respectively.

3. Results and discussion

3.1 SCS and calcination to produce MgO@C precursors

The NPC samples were prepared by the pyrolysis and heat treatment of magnesium nitrate-glycine gels under an inert atmosphere, followed by leaching with acid solution, as shown in Figure 1. The pyrolysis of the nitrate-glycine gels is a well-known SCS process. The glycine-nitrate-based SCS is an exothermic and self-sustaining redox reaction process, which is ignited at around 150–300 °C with the emission of a large amount of gases by heating the mixture of metal nitrates and glycine fuel. This approach has been used to synthesize a variety of functional oxides, such as perovskite catalysts [42-44] and cathode/anode materials for LIBs [45-48]. The conventional SCS process is always performed under an air atmosphere at a stoichiometric ratio (ϕ) close to 1 since that this process is typically used to produce oxide materials. Here, ϕ is the ratio between the total valences of glycine fuel and the total valences of nitrate oxidizers, as described in previous studies[42, 45]. ϕ = 1 indicates a stoichiometric mixture, ϕ < 1 indicates an insufficient fuel condition, and ϕ > 1 indicates an excess fuel condition. Because the purpose of this study was to prepare porous carbon, we employed the glycine-nitrate-based SCS process under Ar atmosphere to produce MgO@C precursors.

Here, $Mg(NO_3)_2$ was used as the raw material to obtain MgO and an excess amount of glycine was used as the carbon source. After being carbonized at a high temperature, the MgO template was removed by acid washing to create numerous pores in the carbon matrix. Three precursor samples were prepared by using different ratios (n2, n2.5, and n3) of glycine to nitrate, and the corresponding ϕ values were calculated to be 1.8, 2.25, and 2.7, which represented high fuel-rich condition.

The temperature history of the SCS reaction was monitored by inserting a K-type thermocouple into the reactants as-loaded in an alumina crucible, as shown in the apparatus setup in Figure S1 (Supplementary Information, SI). Figure S2-(a) presents the temperature history for the SCS reaction at different fuel ratios. With the increase of fuel ratio from n2 to n2.5 and n3, the SCS reaction auto-ignited at increased temperature from ~256 °C to 298 °C and 310 °C, respectively. The sharp temperature jumping increase at ~256 °C for sample n2 represented the typical exothermic SCS reaction. This kind of exothermic reaction was also confirmed by using TG-DTA analysis as shown in Figure S2-(b). It was also observed that the SCS reaction become gentler with the increase of fuel ratio due to addition of increasing amount of fuel. At fuel ratio of n2, the sample was flashed with scattered ashes; at n2.5 and n3, the samples after SCS were comprised in the crucible in the form of a puffy foam, which was very easy to be pulverized.

The SCSed precursors were roughly pulverized and annealed at 800−1100 ^{o}C for 2 h under Ar flow. Figure 2-(a,c,e) shows the XRD patterns of the samples after calcination. The obvious peaks in the XRD patterns for all samples can be indexed to a MgO phase (JCPDS No: 00-004-0829) with good crystallinity. The only difference in phase composition for these calcined sample is that sample NPC-n3-900 contains an

impurity phase $MgCN_2$ (JCPDS No: 00-051-0540).[49, 50] This is due to the supplying of more nitrogen source at n3 for the formation of $MgCN_2$. It is noted that the completeness of combustion redox reaction is in a sequence of n2>n2.5>n3 based on the calculation of ϕ, therefore, after SCS process n3 precursor contains more the largest amount of nitrogen. Calcination temperature is also very important for the formation of $MgCN_2$, 800 ^oC is not high enough for the formation of $MgCN_2$; at the same time, if the calcination temperature is too high, for example at 1000 ^oC, the nitrogen source is also leached quickly, reducing the possibility of forming $MgCN_2$ which needs nitrogen; therefore, a small amount of $MgCN_2$ appears in sample NPC-n3-900 after calcination.

The obtained MgO@C composites were further used for morphology and structure observation using SEM and TEM. Figure S3 shows the SEM images for the samples at different magnification. The samples are composed of highly porous particles with irregular shapes and sizes in the order of several dozens of nanometers to several tens of microns. Meso- and macropores of several tens of nanometers to several hundreds of nanometers are observed in the particles. The porous characteristic is greater for samples n2 and n2.5 than that of sample n3. These meos-macro-pores were formed during the SCS process because of the emission of a large amount of gases accompanying the fast and self-sustaining exothermic reaction, which is a feature of such a process. The porous structure and crystal size of MgO were further confirmed by TEM as shown in Figure S4. A highly three-dimensional porous characteristic with interconnected meso-macro-pores is confirmed for samples n2 and n2.5 as-presented in TEM images (a) and (e). High resolution TEM images (b, d, f, h) for samples n2 and n2.5 indicate that MgO nanocrystals, which have size of several nanometers to dozens of nanometers, are embedded in the carbon matrix. The fast-fourier-transform (FFT)

diffraction patterns for selected areas of samples n2 (images b) and n2.5 (image f) are shown in images (c) and (g), respectively. Each symmetric diffraction spots could represent a MgO grain. Comparing the number of diffraction spots for images (c) and (g), we can conclude that in the same dimension sample n2 has much more MgO grains than sample n2.5. The crowded and overlapped crystals for sample n2 also have larger size than sample n2.5 as confirmed in their high-resolution images. Quite differently, sample n3, as shown in image (i), presents many cubic MgO particles as-embedded in the carbon matrix. The formation of cubic MgO particles for sample n3 is due to the weak and insufficient SCS reaction, which requires higher ignition temperature and the magnesium nitrate precursor or immediate might melt and agglomerate. In contrast, the fast and intensive SCS reaction as-ignited at lower temperatures for samples n2 and n2.5 introduces a sufficient pyrolysis of magnesium nitrate and glycine in a short period, which hence introduces a good mixing of the resulting MgO and carbon. The distribution of MgO crystals in carbon matrix influence the feature of the obtained carbon after acid etching, as will be discussed in following section.

In order to confirm the carbon contents in the MgO@C composites, the samples were air-combusted in a TG analyzer under air flow, as shown in Figure S5. The carbon percentages in the composites are determined from the weight loss from 200 to 700 ^{o}C. Based on these ratios, the theoretical yields were calculated in a unit of g-carbon/g-glycine for these samples, as summarized in Table S1.

3.2 Porous carbon after acid washing

To obtain the final NPC samples, the above MgO@C composites were leached

with HCl solution to remove soluble substances. XRD patterns of the final samples are shown in Figure 2 (b, d, f). There is one broad peak at approximately 25 ° for each sample, corresponding to the (002) plane of graphitic carbon. These patterns of the carbon materials suggest the low graphitization degree. Raman spectroscopy has been widely used to characterize carbon materials and is sensitive to slight changes of C-C bonds of carbon materials. As presented in Figures 3 and S6, a prominent D-band is located at approximately 1350 cm^{-1}, which is associated with a defective or disordered carbon structure. The typical G-band at approximately 1585 cm^{-1} is referred to the ordered sp2 bonded graphitic carbon. Generally, the intensity ratio of D-band to G-band (I_D/I_G) represents the disorder degree of carbon materials. The I_D/I_G ratios of these samples are determined to be larger than 1, representing the great disordering of the as-prepared samples. Especially, with the increase of calcination temperature for samples NPC-n2.5, the intensity ratio based on area is decreased from 2.58, 2.54, 2.39, to 2.27 for the samples calcined at 800, 900, 1000 and 1100 ^oC, respectively, representing the enhanced graphitization with increasing calcination temperature.

The functional groups and bonding characteristics of the NPCs were further evaluated using XPS, which are shown in Figure 4 and S6-2. The survey XPS spectra of the samples, in Figure 4-(a) and S6-2-(a,b), display three peaks at 285.1, 399.3 and 534.2 eV, corresponding to C 1s, N 1s and O 1s, respectively. All NPC samples contain dopants of N and O. The elemental composition is presented in Table 1. The atomic percentage of N and O in the carbon samples are quite dependent on the calcination temperature and glycine ratio. The amount of O-dopant decreases with the increase of calcination temperature, but does not vary too much with the glycine ratio. For N-dopant, with increasing the calcination temperature from 800 to 1100 °C, taking the

samples at n2.5 as the example, the N content decreases from 12.4% to 0.7%, respectively. This is due to the commonly known high-temperature leaching effect, making the release of bonded nitrogen and oxygen at high temperature. Glycine ratio is another parameter to influence the amount of bonded nitrogen in the final NPC. At a calcination temperature of 900 °C for the samples with different glycine ratios, the samples show a larger N content at lower glycine ratio (a content sequence for nitrogen at 900 °C is n2>n2.5>n3). This is because of that, at a higher glycine ratio, $MgCN_2$ was also formed which could consume more N from originally N-C bonded one. However, at a very high temperature of 1000 °C, these samples show similar N amount due to the severe decomposition of N for all samples.

The high-resolution spectra for C 1s, O 1s and N 1s are also presented in Figure 4 and Figure S6. The C 1s spectra can be fitted into three peaks centered at around 284.7, 286.1 and 288.5 eV, corresponding to the C-C or C-H, C-N and/or C-O, and O=C-C bonding, respectively. The O 1s spectra can be divided into two peaks at around 532.0 and 533.5 eV, referring to the C=O and C-O (C-OH or C-O-C) bonds, respectively. [51] With the increase of calcination temperature, the samples present increased ratio of C-O group and decreased ratio of C=O group, as summarized in Table 1. The high-resolution N 1s spectra of the NPC samples are shown in Figure 4 (d, e, f). Totally, the N 1s spectra can be divided into three individual peaks, representing the pyridinic N (~398.5 eV), pyrrolic N (~400.0 eV), and quaternary N (graphitic N, ~401.3 eV).[22, 37, 52] The ratio of these N species are manily influenced by calcination temperature, as a result, the N species show an increased ratio of graphitic N with temperature, indicating the enhanced graphitization at higher temperature. The summary of the N conents and N species are shown in Table 1.

The typical morphology information for the porous carbon samples were obtained from SEM and TEM observation, as shown in Figure 5 and S7. From the SEM images, we can confirm that the carbon samples are comprised of irregular bulk particles in the order of dozens of nanometers to several tens of microns. Meso-macro-pores of several tens of nanometers to several microns are found in the bulk materials, and the as-prepared carbon materials have a loose structure. As described previously, these meso-macropores were created in the SCS process, which emitted a large amount of gases during pyrolysis. From the careful observation using TEM, it is further confirmed that the carbon samples have a highly porous architecture which contains hierarchical multi-pores of interconnected macro-, meso- and micro-pores. The selected area electron diffraction (SAED) pattern of the carbon sample indicated a typical amorphous carbon structure. From the high-resolution TEM images, it is confirmed that the carbon sample is highly defective although some distorted lattice fringes corresponding to the carbon (002) plane could be seen. In addition, many micropores (< 2 nm) and mesopores of several nanometers could be found in the thin carbon layers.

The SSA, pore volume and pore size distribution of the carbon materials were measured by nitrogen absorption-desorption experiment. The adsorption isotherms and pore size distribution curves are shown in Figure 6. The nitrogen adsorption isotherms (Figure 6-(a, d, g)) for the porous carbon samples illustrate the hysteresis type curves with large adsorption at both low and high relative pressure sides, which indicates the coexisting of micropores, mesopores and macropores. The strong nitrogen adsorption occurring at relative pressure near 0 is caused by the presence of micropores; the obvious hysteresis loops between the absorption and desorption branches at ~0.5–0.9 P/P_0 indicate the existence of mesopores; while the steep adsorption at relative pressure

of ~0.9–1.0 demonstrates the presence of macropores. The SSA of the samples are evaluated using the BET method and t-method for the distinction of external mesopores and internal micropores. The total pore volumes of the samples are indicated by the pore volumes at P/P_o = 0.95 and 0.99, respectively. Here, the pore volume at 0.95 corresponds to pores up to around 40 nm, while the pore volume at 0.99 corresponds to pores up to around 200 nm. Furthermore, from the difference of these two values, we can also briefly estimate the macropore volume of the samples. The micropore volume is obtained by t-method, while the mesopore volume is calculated by the pore volume at 0.95 subtracting the micropore volume. The above structural parameters for the porous carbons are summarized in Table 2. The pore size distribution is analyzed by both BJH and NLDFT methods, as shown in Figure 6-(b, e, h) and (c, f, i), respectively.

The porous characteristics of the carbon samples are mainly influenced by the calcination temperature and glycine-nitrate ratio. As increasing the calcination temperature, the total SSA for the samples prepared at the same glycine-nitrate ratio do not change too much, but the volume and number of micropores are decreased at higher calcination temperatures due to the crystal growth of MgO and sintering of micropores. For the samples prepared at the same calcination temperature and decreasing glycine-nitrate ratio, the carbon samples show both increased SSA and pore volumes (both micropore and mesopore), which are caused by the increased ratio of MgO pore creators as-dispersed in the carbon matrix.

Such a hierarchical multi-porous architecture is highly desirable for electrochemical energy storage and conversion because it allows fast ion diffusion by shortening the diffusion pathways, where macroporous frameworks may be used as ion-buffering reservoirs, mesoporous walls as ion highways for fast ion transmission

and microporous textures for charge accommodation. [22, 35, 53-55] The new process of this work for producing porous carbon indicates many advantages such as: 1) possibility of easy scaling-up since only low-cost raw materials and simple equipment are employed; 2) additional activation process is not required which is different from the conventional process that normally contains a KOH etching process even that KOH is quite corrosive to the equipment; 3) products with unique porous structures containing hierarchical multi-pores and high SSA, which is also controllable by adjusting the experiment condition especially the glycine to nitrate ratio.

3.3 Electrochemical performance as ORR electrocatalyst

The electrochemical catalytic properties for the porous carbon were characterized by RDE method performed in 0.1 M KOH electrolyte, and the results are shown in Figures 7, S8 and S9. The measurements were carried out for the samples in two series in terms of their preparation parameters including calcination temperature and glycine-nitrate ratio, thereby to find an optimal preparation condition for a best ORR catalyst. Firstly, CV analysis was carried out in both Ar and O_2-saturated electrolyte at a scan rate of 50 mV s^{-1}, which is illustrated in Figure 7-(a, b, c). In the O_2-saturated electrolyte, it is observed that obvious cathodic ORR peaks appear near 0.8 V vs. RHE, which are quite different to the CV curves in Ar-saturated electrolyte showing featureless curves.

Figure 7-(d) shows the LSV curves for sample NPC-n2-1000 obtained under varying rotation speeds, while the LSV curves for other samples are presented in Figure S8. Based on this, the K-L plots are simulated as shown in Figures 7-(e) and S9. The

comparison of the LSV curves at the same rotation speed of 1600 rpm are shown in Figure 7-(f, g, h). The influence of calcination temperature to the ORR activity is compared using samples NPC-n2.5 in Figure 7-(f), and it is concluded that 1000 ^{o}C is the best calcination temperature which can offer an electrocatalyst with highest activity in terms of higher onset potential and half-wave potential, as summarized in Table S2. This is because of that there is a trade-off relationship between the conductivity requiring a higher calcination temperature and inevitable concurrent nitrogen leaching effect at higher calcination temperature. When comparing the electron transfer number as-derived from the K-L plots (in Table S3 and Figure S9-(j,k,l)), it is found that the samples calcined at 900 and 1000 ^{o}C present higher values (approaching 4) than those for the samples obtained at 800 and 1100 ^{o}C. Calcination temperature mainly affect the graphitization degree, nitrogen dopant amount and nitrogen species, which has been carefully discussed by the results of Raman spectroscopy and XPS. At a low calcination temperature, especially 800 ^{o}C, although the nitrogen dopant amount is high, the sample is not well carbonized, introducing a low electric-conductive and structure-unstable sample, therefore, the ORR activity is low for the samples calcined at low temperature. However, a very high calcination temperature of 1100 ^{o}C induce a significant release of the nitrogen dopant, making the severe decrease of active sites of N-C for ORR.

Another important production parameter that will greatly influence the ORR properties is the glycine-nitrate ratio. The samples prepared with different glycine-nitrate ratios and calcined at the same temperatures of 900 and 1000 ^{o}C are compared in Figure 7-(g, h). It is observed that the ORR activities decrease in the following sequence NPC-n2 > NPC-n2.5 > NPC-n3 at each temperature, which is also greatly higher than that of KB. This tendency is mainly caused by the decreased SSA of

the obtained NPCs with the increase of glycine ratio.

Sample NPC-n2-1000 shows the best ORR activity, which is ascribed to the balance of high graphitization degree, optimized nitrogen content and species, the hierarchical porous structure and its highest SSA. The activity of NPC-n2-1000 is even superior than that of Pt/C as-evaluated in many literatures, which is also among the best carbon-based ORR catalysts in the recent reports.[22, 24, 36, 56-59]

In addition to the good eletrocatalytic activity, the NPC electrode also exhibits high durability as shown in Figure 8-(a), which is examined by chronoamperometric method as-conducted at -0.4 V vs. Ag/AgCl in O_2-saturated KOH solution at a rotation speed of 1600 rpm. The NPC-n2-1000 electrode can retain almost 100% of its original current density after 10 h's holding. The durability of our NPC is quite superior than that of commercial Pt/Cs, which degrade about 10-50% after 10 h in the literatures.[26, 39, 49, 57] Moreover, it is also important to evaluate the methanol tolerance of the catalysts since in the practical application of fuel cells, the crossover effect of small-molecule organic fuels, such as methanol, is an important consideration for cathode materials. It is well known that Pt/C catalysts are not tolerant to methanol poisoning.[26, 39, 49, 57] However, our NPC can show a high tolerance to methanol crossover, as illustrated in Figure 8-(b). The measurement was conducted by chronoamperometry at -0.4 V vs. Ag/AgCl in O_2-saturated KOH solution at a rotation speed of 1600 rpm, in which 2 vol.% methanol was added in the electrolyte. The NPC-n2-1000 electrode presents a slight decrease of current density after the addition of methanol, which indicates the superior fuel selectivity toward ORR for the NPC sample, making it a promising cathodic catalyst for alkaline direct methanol fuel cells.

3.4 Electrochemical performance as EDLC electrode

The electrochemical properties of the NPCs for EDLC were evaluated in a symmetric two-electrode cell. CV and galvanostatic charge/discharge measurements were conducted with a 6 M KOH electrolyte. Figure 9-(a) and Figure S10 present the CV curves for the symmetric cells at various scanning rate. The CV curves for the all samples, excluding NPC-n2.5-800, illustrate symmetrical rectangular shapes from 5 to 100 mV s^{-1}, indicating the ideal double-layer capacitance behavior for the NPCs. Sample NPC-n2.5-800 shows deformed CV curves, especially at high scanning rate, which is due to its low graphitization degree as-calcined at a low temperature. Galvanostatic charge/discharge measurement was conducted at varying current densities from 1 to 10 A g^{-1}, with the typical profiles shown in Figure 9-(b,c) and Figure S12. The charge/discharge curves (excluding sample NPC-n2.5-800) show symmetric triangular shapes, illustrating the typical supercapacitive behavior of the NPCs with excellent capacitive reversibility, which is in well agreement with the CV measurement. Figure 9-(d,e,f) present the gravimetric capacitances at varying current densities. These values of capacitances are similar to those as-calculated from CV curves in Figure S11. Among these samples, NPC-n2-900 presents the highest capacitances, i.e., 232, 224, 219, 213, 209, and 205 F g^{-1} at discharge current densities of 1, 2, 3, 5, 7 and 10 A g^{-1}, respectively. Generally, high SSA, superior pore structure, highly active heteroatoms and good electric conductivity are beneficial for carbon-based supercapacitors. As for the samples prepared at different temperatures, it can be concluded that 900 ^{o}C is best for producing NPC with the highest capacitance, in which the NPC sample can have a good balance of graphitization degree, nitrogen-doping, oxygen-doping and high SSA. At a temperature

lower than 900 ^{o}C, the sample is not well carbonized, making an unstable and electrically low-conductive sample. At the same time, if the temperature is too high, the doping amount of nitrogen and oxygen are decreased greatly, making a decreased capacitance. For the samples prepared under the same calcination temperature (900 or 1000 ^{o}C), the capacitance of the samples shows a decreasing tendency of NPC-n2 > NPC-n2.5 > NPC-n3, which is mainly caused by their decreasing SSA of the NPCs. The NPC samples, excluding NPC-n2.5-800, also present very high cycling stability at a current density of 2 A g^{-1} over 10000 cycles, as shown in Figure 9-(g,h,i). After 10000 cycles' cycling, sample NPC-n2-900 can still present a high capacitance of 180 F g^{-1}.

The specific capacitances in a unit of F m^{-2} are also calculated, as shown in Table S4. For the samples prepared at the same glycine ratio but under different calcination temperature, for example NPC-n2.5-900, NPC-n2.5-1000 and NPC-n2.5-1100 (excluding NPC-n2.5-800), these samples have very similar SSA, similar pore volume and similar pore size distribution, which is also similar to those of KB. It is observed that with the increasing amount of nitrogen and oxygen-doping, the NPCs show both increased total capacitance and specific capacitance, which is greatly higher than the non-nitrogen-doped KB. This is caused by the positive effect of nitrogen and oxygen-doping, contributing to the increase of extra pseudocapacitance.[32, 51] For the same reason, NPC-n2-900 and NPC-n3-900 also present both higher total capacitance and specific capacitance than those of sample NPC-n2-1000 and NPC-n3-1000, respectively. We also compare the samples that are calcined under the same temperature (900 or 1000 ^{o}C) but at different glycine ratio, it is concluded that with the increase of nitrogen and oxygen content, the total capacitance increases; with the increase of SSA, the total capacitance also increases; however, the specific capacitance is not

proportionate to the total SSA nor the nitrogen content. For example, for samples NPC-n2-1000, NPC-n2.5-1000 and NPC-n3-1000, they have similar nitrogen content but different SSA and different pore size distribution; sample NPC-n2-1000 has the highest SSA and highest total capacitance, but it has the lowest specific capacitance. At the same time, for samples NPC-n2-900, NPC-n2.5-900 and NPC-n3-900, they have different nitrogen content, different SSA and different pore size distribution; high nitrogen content and high SSA might contribute to a high capacitance, thereby NPC-n2-900 present the largest total capacitance; however, this sample shows the lowest specific capacitance. This is because of that not all the pore surface areas are efficiently used, especially for the small micropores, due to the occurrence of ion-blockage within the small pores, although such a sample has a very high SSA.

The high electrochemical performance of the NPCs for EDLC is due to their hierarchical porous structure, nitrogen/oxygen-doping and high SSA. The hierarchical pore structure of the NPC can provide a fast mass transport on a large electrode/electrolyte interfaces for charge-transfer reactions and offer an easy ion transport by reducing the ion-transport diffusion distance, ultimately leading to the high-rate supercapacitance. Moreover, the high SSA and abundant nitrogen/oxygen-dopants of NPCs can provide plenty active sites for charge storage, which significantly increase their capacitance. Finally, the heteroatom-doping also increase the wettability of electrode materials, facilitating the electrolyte ions to easily access. All the above features of NPCs are highly desirable for their performance improvement for energy storage devices

4. Conclusions

In summary, NPC was synthesized by a facile MgO template method as-mediated by a SCS process. The MgO@C precursor was prepared by a facile and scalable glycine-nitrate-based SCS with subsequent calcination. After acid washing, NPC was obtained, which contained macropores, mesopores and micropores. The macropores and large mesopores were formed during the SCS process, whereas the small mesopores and micropores were created by removing the MgO template. Because of the synergistic effect of the high surface area, interconnected hierarchical multi-pores and nitrogen-doping, the NPC demonstrated good performance as both ORR electrocatalyst and EDLC electrode materials. Due to the unique porous structure and facile synthesis for NPC, the sample may also show promising applications in Li-ion batteries and pollutant absorbent.

Acknowledgements

This work is supported partially by Nippon Sheet Glass Foundation for Materials Science and Engineering, and JSPS KAKENHI (Grant Number 18K14047). The authors also thank the “Nanotechnology platform” Program of the Ministry of Education, Culture, Sports, Science and Technology (MEXT) for the use of analysis equipment.

References

[1] C. Zhang, W. Lv, Y. Tao, Q.-H. Yang, Towards superior volumetric performance: design and preparation of novel carbon materials for energy storage, Energy & Environmental Science 8 (2015) 1390-1403.

[2] L.L. Zhang, X.S. Zhao, Carbon-based materials as supercapacitor electrodes, Chemical Society Reviews 38 (2009) 2520-2531.

[3] A. Borenstein, O. Hanna, R. Attias, S. Luski, T. Brousse, D. Aurbach, Carbon-based composite materials for supercapacitor electrodes: a review, Journal of Materials Chemistry A 5 (2017) 12653-12672.

[4] W.Y. Long, B.Z. Fang, A. Ignaszak, Z.Z. Wu, Y.J. Wang, D. Wilkinson, Biomass-derived nanostructured carbons and their composites as anode materials for lithium ion batteries, Chemical Society Reviews 46 (2017) 7176-7190.

[5] M. Sevilla, R. Mokaya, Energy storage applications of activated carbons: supercapacitors and hydrogen storage, Energy & Environmental Science 7 (2014) 1250-1280.

[6] Y. Noh, Y. Kim, S. Lee, E.J. Lim, J.G. Kim, S.M. Choi, M.H. Seo, W.B. Kim, Exploring the effects of the size of reduced graphene oxide nanosheets for Pt-catalyzed electrode reactions, Nanoscale 7 (2015) 9438-9442.

[7] H. Hyunsu, N. Yuseong, K. Yoongon, Y.V.S. K., P. Seongmin, Y. Wongeun, L. Seungjun, K.W. Bae, Electrocatalytic Oxidations of Formic Acid and Ethanol over Pd Catalysts Supported on a Doped Polypyrrole‐Carbon Composite, ChemistrySelect 2 (2017) 6260-6268.

[8] C. Zhu, T. Akiyama, Cotton derived porous carbon via an MgO template method for high performance lithium ion battery anodes, Green Chemistry 18 (2016) 2106-2114.

[9] M. Chen, S. Jiang, S. Cai, X. Wang, K. Xiang, Z. Ma, P. Song, A.C. Fisher, Hierarchical porous carbon modified with ionic surfactants as efficient sulfur hosts for the high-performance lithium-sulfur batteries, Chemical Engineering Journal 313 (2017) 404-414.

[10] T.Y. Liu, F. Zhang, Y. Song, Y. Li, Revitalizing carbon supercapacitor electrodes with hierarchical porous structures, Journal of Materials Chemistry A 5 (2017) 17705-17733.

[11] M. Yang, Z. Zhou, Recent Breakthroughs in Supercapacitors Boosted by Nitrogen-Rich Porous Carbon Materials, Adv. Sci. 4 (2017) 10.

[12] R.-J. Mo, Y. Zhao, M.-M. Zhao, M. Wu, C. Wang, J.-P. Li, S. Kuga, Y. Huang, Graphene-like porous carbon from sheet cellulose as electrodes for supercapacitors, Chemical Engineering Journal 346 (2018) 104-112.

[13] L. Zhu, F. Shen, R.L. Smith, L. Yan, L. Li, X. Qi, Black liquor-derived porous carbons from rice straw for high-performance supercapacitors, Chemical Engineering Journal 316 (2017) 770-777.

[14] Y. Gong, D. Li, C. Luo, Q. Fu, C. Pan, Highly porous graphitic biomass carbon as advanced electrode materials for supercapacitors, Green Chemistry 19 (2017) 4132-4140.

[15] N. Guo, M. Li, X. Sun, F. Wang, R. Yang, Enzymatic hydrolysis lignin derived hierarchical porous carbon for supercapacitors in ionic liquids with high power and energy densities, Green Chemistry 19 (2017) 2595-2602.

[16] R. Berenguer, F.J. Garcia-Mateos, R. Ruiz-Rosas, D. Cazorla-Amoros, E. Morallon, J. Rodriguez-Mirasol, T. Cordero, Biomass-derived binderless fibrous carbon electrodes for ultrafast energy storage, Green Chemistry 18 (2016) 1506-1515.

[17] H. Fan, W. Shen, Gelatin-Based Microporous Carbon Nanosheets as High Performance Supercapacitor Electrodes, ACS Sustainable Chemistry & Engineering 4 (2016) 1328-1337.

[18] C.Z. Zhu, H. Li, S.F. Fu, D. Du, Y.H. Lin, Highly efficient nonprecious metal catalysts towards oxygen reduction reaction based on three-dimensional porous carbon nanostructures, Chemical Society Reviews 45 (2016) 517-531.

[19] P.F. Zhang, H.Y. Zhu, S. Dai, Porous Carbon Supports: Recent Advances with Various Morphologies and Compositions, ChemCatChem 7 (2015) 2788-2805.

[20] H.C. Yang, J. Liang, Z.X. Wang, B.G. An, F. Li, Applications of porous carbon materials in the electrocatalysis of the oxygen reduction reaction, New Carbon Mater. 31 (2016) 243-263.

[21] A. Elmouwahidi, J.F. Vivo-Vilches, A.F. Pérez-Cadenas, F.J. Maldonado-Hódar, F. Carrasco-Marín, Free metal oxygen-reduction electro-catalysts obtained from biomass residue of the olive oil industry, Chemical Engineering Journal 306 (2016) 1109-1115.

[22] H.-W. Liang, X. Zhuang, S. Brüller, X. Feng, K. Müllen, Hierarchically porous carbons with optimized nitrogen doping as highly active electrocatalysts for oxygen reduction, Nature Communications 5 (2014) 4973.

[23] H.T. Chung, D.A. Cullen, D. Higgins, B.T. Sneed, E.F. Holby, K.L. More, P. Zelenay, Direct atomic-level insight into the active sites of a high-performance PGM-free ORR catalyst, Science 357 (2017) 479-484.

[24] Y. An, Z. Li, Y. Yang, B. Guo, Z. Zhang, H. Wu, Z. Hu, Synthesis of Hierarchically Porous Nitrogen‐Doped Carbon Nanosheets from Agaric for High‐Performance Symmetric Supercapacitors, Advanced Materials Interfaces 4 (2017) 1700033.

[25] Y.Y. Smolin, K.L.V. Aken, M. Boota, M. Soroush, Y. Gogotsi, K.K.S. Lau, Engineering Ultrathin Polyaniline in Micro/Mesoporous Carbon Supercapacitor Electrodes Using Oxidative Chemical Vapor Deposition, Advanced Materials Interfaces 4 (2017) 1601201.

[26] H. Zhao, C.-C. Weng, Z.-P. Hu, L. Ge, Z.-Y. Yuan, CdS-Polydopamine-Derived N,S-Codoped Hierarchically Porous Carbons as Highly Active Electrocatalyst for Oxygen Reduction, ACS Sustainable Chemistry & Engineering 5 (2017) 9914-9922.

[27] D.-W. Wang, D. Su, Heterogeneous nanocarbon materials for oxygen reduction reaction, Energy & Environmental Science 7 (2014) 576-591.

[28] J.-S.M. Lee, M.E. Briggs, C.-C. Hu, A.I. Cooper, Controlling electric double-layer capacitance and

pseudocapacitance in heteroatom-doped carbons derived from hypercrosslinked microporous polymers, Nano Energy 46 (2018) 277-289.
[29] J. Zhu, D. Xu, W. Qian, J. Zhang, F. Yan, Heteroatom-Containing Porous Carbons Derived from Ionic Liquid-Doped Alkali Organic Salts for Supercapacitors, Small 12 (2016) 1935-1944.
[30] J. Zhang, Z. Xia, L. Dai, Carbon-based electrocatalysts for advanced energy conversion and storage, Science Advances 1 (2015).
[31] L. Miao, D. Zhu, M. Liu, H. Duan, Z. Wang, Y. Lv, W. Xiong, Q. Zhu, L. Li, X. Chai, L. Gan, Cooking carbon with protic salt: Nitrogen and sulfur self-doped porous carbon nanosheets for supercapacitors, Chemical Engineering Journal 347 (2018) 233-242.
[32] Z. Ye, F. Wang, C. Jia, K. Mu, M. Yu, Y. Lv, Z. Shao, Nitrogen and oxygen-codoped carbon nanospheres for excellent specific capacitance and cyclic stability supercapacitor electrodes, Chemical Engineering Journal 330 (2017) 1166-1173.
[33] Z. Huang, Z. Liao, W. Yang, H. Zhou, C. Fu, Y. Gong, L. Chen, Y. Kuang, Different types of nitrogen species in nitrogen-doped carbon material: The formation mechanism and catalytic role on oxygen reduction reaction, Electrochimica Acta 245 (2017) 957-966.
[34] T. Huang, S. Mao, M. Qiu, O. Mao, C. Yuan, J. Chen, Nitrogen-boron Dipolar-doped Nanocarbon as a High-efficiency Electrocatalyst for Oxygen Reduction Reaction, Electrochimica Acta 222 (2016) 481-487.
[35] Y.-Q. Zhao, M. Lu, P.-Y. Tao, Y.-J. Zhang, X.-T. Gong, Z. Yang, G.-Q. Zhang, H.-L. Li, Hierarchically porous and heteroatom doped carbon derived from tobacco rods for supercapacitors, Journal of Power Sources 307 (2016) 391-400.
[36] Y. Wang, S. Zuo, Y. Liu, Ammonia modification of high-surface-area activated carbons as metal-free electrocatalysts for oxygen reduction reaction, Electrochimica Acta 263 (2018) 465-473.
[37] R. Ma, Y. Zhou, P. Li, Y. Chen, J. Wang, Q. Liu, Self-Assembly of Nitrogen-doped Graphene-Wrapped Carbon Nanoparticles as an Efficient Electrocatalyst for Oxygen Reduction Reaction, Electrochimica Acta 216 (2016) 347-354.
[38] Z. Zhang, T. Cao, S. Liu, X. Duan, L.M. Liu, S. Wang, Y. Liu, Substrate‐Induced Synthesis of Nitrogen‐Doped Holey Graphene Nanocapsules for Advanced Metal‐Free Bifunctional Electrocatalysts, Particle & Particle Systems Characterization 34 (2017) 1600207.
[39] D. Gu, R. Ma, Y. Zhou, F. Wang, K. Yan, Q. Liu, J. Wang, Synthesis of Nitrogen-Doped Porous Carbon Spheres with Improved Porosity toward the Electrocatalytic Oxygen Reduction, ACS Sustainable Chemistry & Engineering 5 (2017) 11105-11116.
[40] C. Zhu, C. Kim, Y. Aoki, H. Habazaki, Nitrogen-Doped Hierarchical Porous Carbon Architecture Incorporated with Cobalt Nanoparticles and Carbon Nanotubes as Efficient Electrocatalyst for Oxygen Reduction Reaction, Advanced Materials Interfaces 4 (2017) 1700583.
[41] C. Zhu, Y. Aoki, H. Habazaki, Co9S8 Nanoparticles Incorporated in Hierarchically Porous 3D

Few-Layer Graphene-Like Carbon with S,N-Doping as Superior Electrocatalyst for Oxygen Reduction Reaction, Particle & Particle Systems Characterization 34 (2017) 1700296.

[42] C. Zhu, A. Nobuta, I. Nakatsugawa, T. Akiyama, Solution combustion synthesis of LaMO3 (M = Fe, Co, Mn) perovskite nanoparticles and the measurement of their electrocatalytic properties for air cathode, Int. J. Hydrog. Energy 38 (2013) 13238-13248.

[43] C. Zhu, A. Nobuta, Y.-W. Ju, T. Ishihara, T. Akiyama, Solution combustion synthesis of Ce0.6Mn0.3Fe0.1O2 for anode of SOFC using LaGaO3-based oxide electrolyte, Int. J. Hydrogen Energy 38 (2013) 13419-13426.

[44] Z.-X. Wei, Y.-Q. Xu, H.-Y. Liu, C.-W. Hu, Preparation and catalytic activities of LaFeO3 and Fe2O3 for HMX thermal decomposition, Journal of Hazardous Materials 165 (2009) 1056-1061.

[45] C. Zhu, A. Nobuta, G. Saito, I. Nakatsugawa, T. Akiyama, Solution combustion synthesis of LiMn2O4 fine powders for lithium ion batteries, Adv. Powder Technol. 25 (2014) 342-347.

[46] C. Zhu, T. Akiyama, Optimized conditions for glycine-nitrate-based solution combustion synthesis of LiNi0.5Mn1.5O4 as a high-voltage cathode material for lithium-ion batteries, Electrochim. Acta 127 (2014) 290-298.

[47] M.W. Raja, S. Mahanty, R.N. Basu, Filter paper templated interconnected nanocrystalline LiMn2O4 with high coulombic efficiency and rate capability, Journal of Materials Chemistry 19 (2009) 6161-6166.

[48] C.-G. Han, C. Zhu, N. Sheng, Y. Aoki, H. Habazaki, T. Akiyama, A facile one-pot synthesis of FeOx/carbon/graphene composites as superior anode materials for lithium-ion batteries, Electrochimica Acta 235 (2017) 88-97.

[49] L. Qin, R. Ding, H. Wang, J. Wu, C. Wang, C. Zhang, Y. Xu, L. Wang, B. Lv, Facile synthesis of porous nitrogen-doped holey graphene as an efficient metal-free catalyst for the oxygen reduction reaction, Nano Research 10 (2017) 305-319.

[50] U. Berger, W. Schnick, Syntheses, crystal structures, and vibrational spectroscopic properties of MgCN2, SrCN2, and BaCN2, Journal of Alloys and Compounds 206 (1994) 179-184.

[51] F. Hu, J. Wang, S. Hu, L. Li, G. Wang, J. Qiu, X. Jian, Inherent N,O-containing carbon frameworks as electrode materials for high-performance supercapacitors, Nanoscale 8 (2016) 16323-16331.

[52] M. Wu, J. Qiao, K. Li, X. Zhou, Y. Liu, J. Zhang, A large-scale synthesis of heteroatom (N and S) co-doped hierarchically porous carbon (HPC) derived from polyquaternium for superior oxygen reduction reactivity, Green Chemistry 18 (2016) 2699-2709.

[53] J. Ou, Y. Zhang, L. Chen, Q. Zhao, Y. Meng, Y. Guo, D. Xiao, Nitrogen-rich porous carbon derived from biomass as a high performance anode material for lithium ion batteries, Journal of Materials Chemistry A 3 (2015) 6534-6541.

[54] B. Wang, S. Li, X. Wu, J. Liu, J. Chen, Biomass chitin-derived honeycomb-like nitrogen-doped carbon/graphene nanosheet networks for applications in efficient oxygen reduction and robust lithium storage, Journal of Materials Chemistry A 4 (2016) 11789-11799.

[55] S. Dutta, A. Bhaumik, K.C.W. Wu, Hierarchically porous carbon derived from polymers and biomass: effect of interconnected pores on energy applications, Energy & Environmental Science 7 (2014) 3574-3592.
[56] Y. Qiu, J. Huo, F. Jia, B.H. Shanks, W. Li, N- and S-doped mesoporous carbon as metal-free cathode catalysts for direct biorenewable alcohol fuel cells, Journal of Materials Chemistry A 4 (2016) 83-95.
[57] P.-C. Shi, J.-D. Yi, T.-T. Liu, L. Li, L.-J. Zhang, C.-F. Sun, Y.-B. Wang, Y.-B. Huang, R. Cao, Hierarchically porous nitrogen-doped carbon nanotubes derived from core-shell ZnO@zeolitic imidazolate framework nanorods for highly efficient oxygen reduction reactions, Journal of Materials Chemistry A 5 (2017) 12322-12329.
[58] L. Ma, S. Chen, Z. Pei, Y. Huang, G. Liang, F. Mo, Q. Yang, J. Su, Y. Gao, J.A. Zapien, C. Zhi, Single-Site Active Iron-Based Bifunctional Oxygen Catalyst for a Compressible and Rechargeable Zinc–Air Battery, ACS Nano 12 (2018) 1949-1958.
[59] Z. Zhang, X. Gao, M. Dou, J. Ji, F. Wang, Fe-Nx moiety-modified hierarchically porous carbons derived from porphyra for highly effective oxygen reduction reaction, Journal of Materials Chemistry A 5 (2017) 1526-1532.

Table 1. Summary of the XPS analysis

Samples	C content [at%]	O content [at%]	N content [at%]	*Percentage of N species*			*Percentage of O species*	
				Graphitic (~401.3 eV) [%]	Pyrrolic (~400.0 eV) [%]	Pyridinic (~398.5 eV) [%]	C-O (~533.5 eV) [%]	C=O (~532.0 eV) [%]
NPC-n2.5-800	74.3	13.3	12.4	11.9	40.9	47.2	43.3	56.7
NPC-n2.5-900	84.2	11.3	4.5	18.2	39.1	42.7	66.5	33.5
NPC-n2.5-1000	89.8	8.1	2.1	28.8	35.4	35.8	75.5	24.5
NPC-n2.5-1100	84.1	5.2	0.7	49.9	14.6	35.5	95.5	4.5
NPC-n2-900	82.2	11.1	6.7	15.6	39.4	45.0	65.9	34.1
NPC-n2-1000	89.6	7.8	2.6	29.1	33.5	37.4	77.7	22.3
NPC-n3-900	83.9	11.9	4.2	17.9	38.3	43.8	63.9	36.1
NPC-n3-1000	89.7	7.9	2.4	27.6	38.0	34.4	75.2	24.8

Table 2. Porous structural properties of carbon samples as characterized by N_2 adsorption.

Samples	BET SSA [$m^2 g^{-1}$]	a_{total} [$m^2 g^{-1}$]	a_{ex} [$m^2 g^{-1}$]	$a_{micro} = a_{total}-a_{ex}$ [$m^2 g^{-1}$]	$V_{0.99}$ [$cm^3 g^{-1}$]	$V_{0.95}$ [$cm^3 g^{-1}$]	V_{micro} [$cm^3 g^{-1}$]	$V_{meso} = V_{0.95}-V_{micro}$ [$cm^3 g^{-1}$]
NPC-n2.5-800	1378	1432	338	1095	2.6	1.5	0.8	0.7
NPC-n2.5-900	1336	1334	429	905	2.9	1.8	0.9	0.9
NPC-n2.5-1000	1331	1357	400	957	2.8	1.8	1.0	0.8
NPC-n2.5-1100	1249	1272	399	872	3.0	1.9	1.0	0.9
NPC-n2-900	1958	1879	561	1318	3.3	2.3	1.3	1.0
NPC-n2-1000	1838	1790	752	1037	4.3	2.8	1.4	1.4
NPC-n3-900	1030	1062	187	875	1.5	1.0	0.6	0.4
NPC-n3-1000	958	978	226	752	1.4	1.0	0.5	0.5
KB	1330	1303	432	871	3.3	1.7	0.9	0.8

BET SSA: specific surface area as-calculated from the adsorption data by BET method; $V_{0.99}$: total pore volume at P/P_0=0.99, corresponding to the pores with diameters up to around 200 nm; $V_{0.95}$: total pore volume at P/P_0=0.95, corresponding to the pores with diameters up to around 40 nm; a_{total}: the total surface area as-determined by t method; a_{ex}: the external surface area as-determined by t method; a_{micro}: the micropore surface area as-determined by a_{total}-a_{ex}; V_{micro}: the micropore volume as-analyzed by *t* method; V_{meso}: the mesopore volume as-determined by $V_{0.95}$-V_{micro}.

Figure 1. Schematic diagram for the formation process of the hierarchical nitrogen-containing multi-porous carbon.

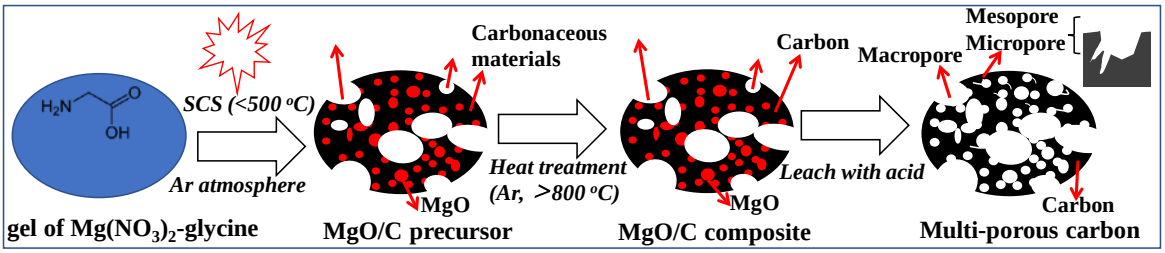

Figure 2. XRD patterns for the samples obtained after calcination (a, c, e) and after acid washing (b, d, f).

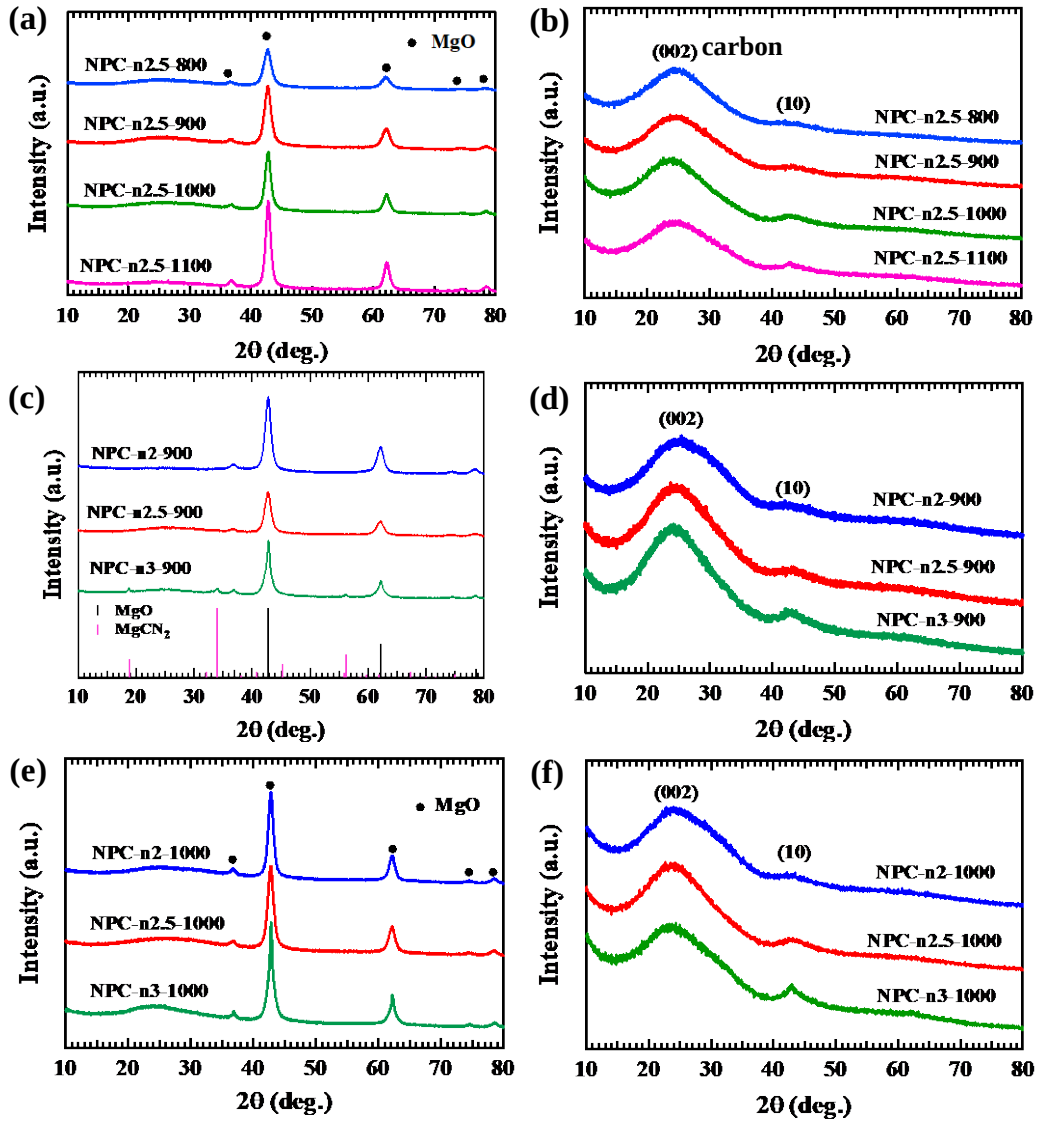

Figure 3. Raman spectra for the carbon samples obtained with different calcination temperature. The Raman spectra for other samples are shown in Figure S6.

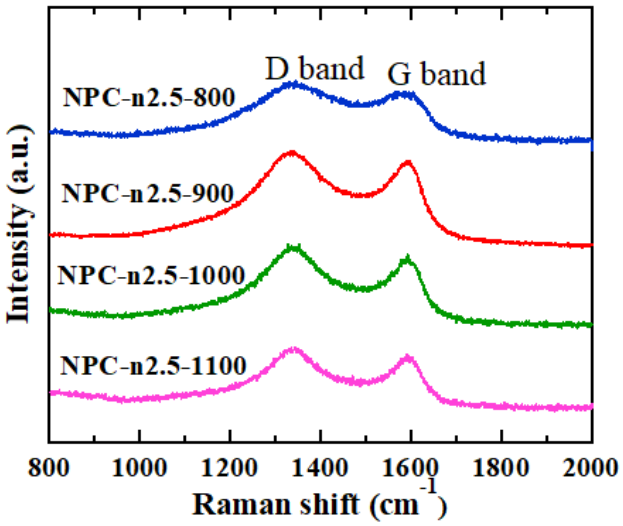

Figure 4. XPS analysis of the obtained carbon samples. (a) The typical wide scan curves; (b) narrow scan of C 1s; (c) narrow scan of O 1s; (d,e,f) narrow scan of N 1s. More spectra are shown in Figure S6-2.

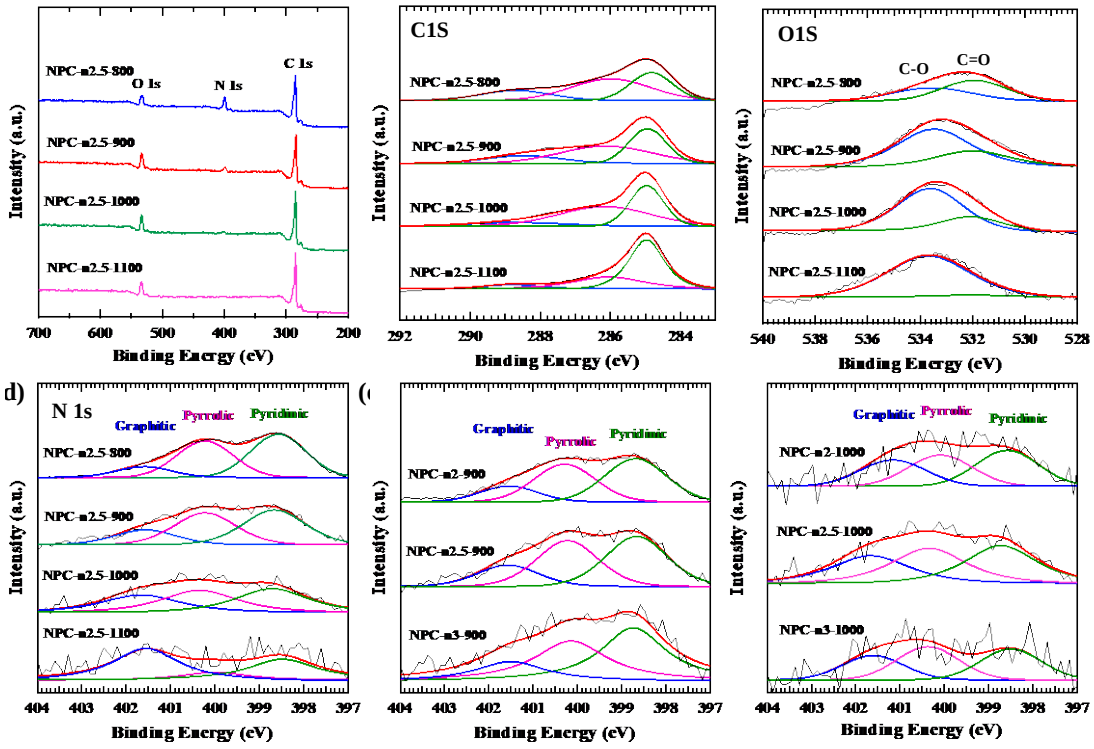

Figure 5. SEM and TEM observation of the typical NPC carbon sample (NPC-n2-1000). (a,b) The typical SEM images; (c,d) the typical TEM image at a low magnification (inset shows the SAED pattern); (e, f) the high-resolution TEM images. More SEM images are shown in Figure S7.

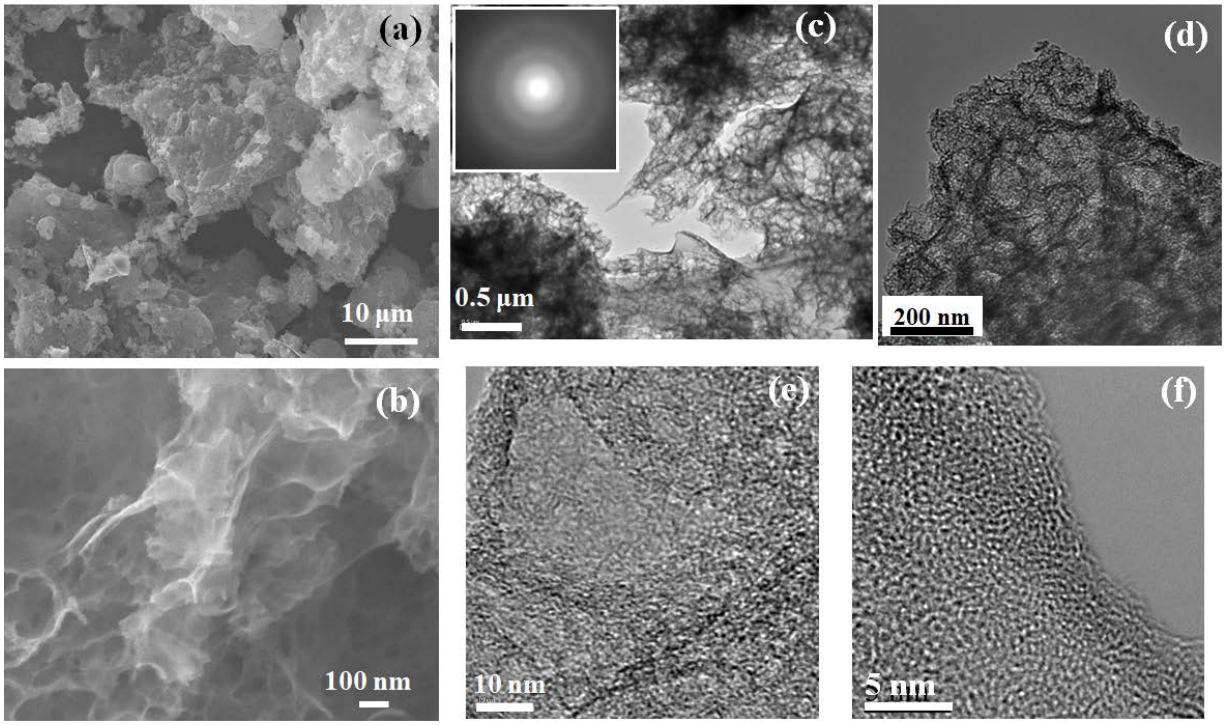

Figure 6. Nitrogen adsorption isotherm (a, d, g), BJH pore size distribution (b, e, h) and NLDFT pore size distribution (c, f, i) of the obtained carbon samples.

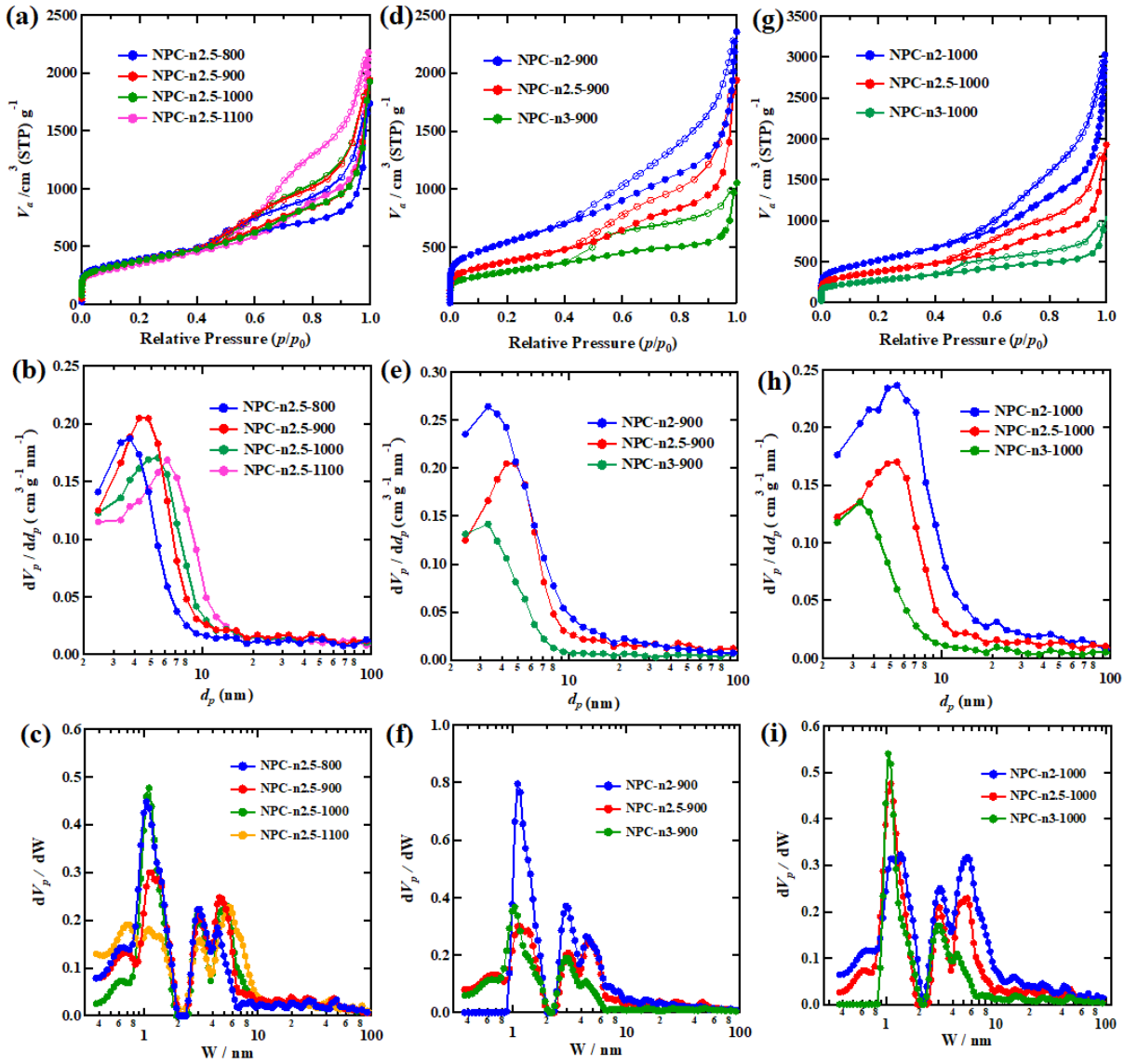

Figure 7. Electrochemical performance of the NPC sample for ORR. (a, b, c) The CV curves in both Ar and O_2-saturated electrolyte at a scan rate of 50 mV s^{-1}; (d) the typical LSV curves at various rotation speeds for NPC-n2-1000; (e) typical K-L plots for NPC-n2-1000; (f, g, h) the LSV curves at a rotation speed of 1600 rpm. More details are shown in Figure S8 and S9. KB is the comparison sample using commercial KETJEN BLACK.

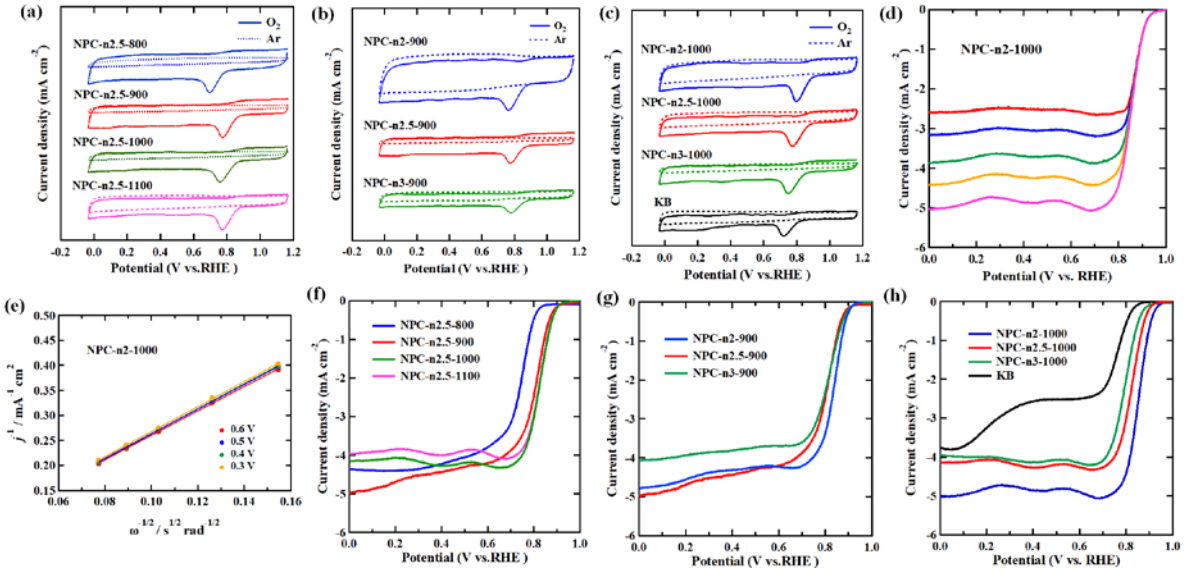

Figure 8. (a) Chronoamperometric responses of NPC-n2-1000 catalyst in O_2-saturated 0.1 M KOH and (b) chronoamperometric responses of NPC-n2-1000 showing the effect of adding methanol.

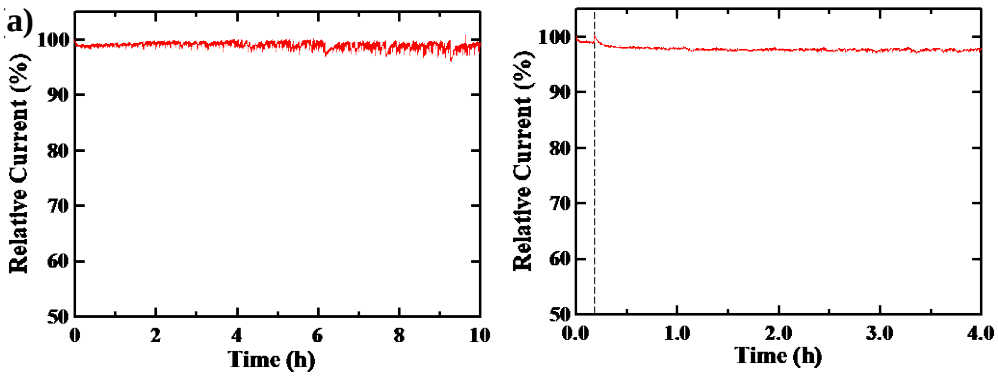
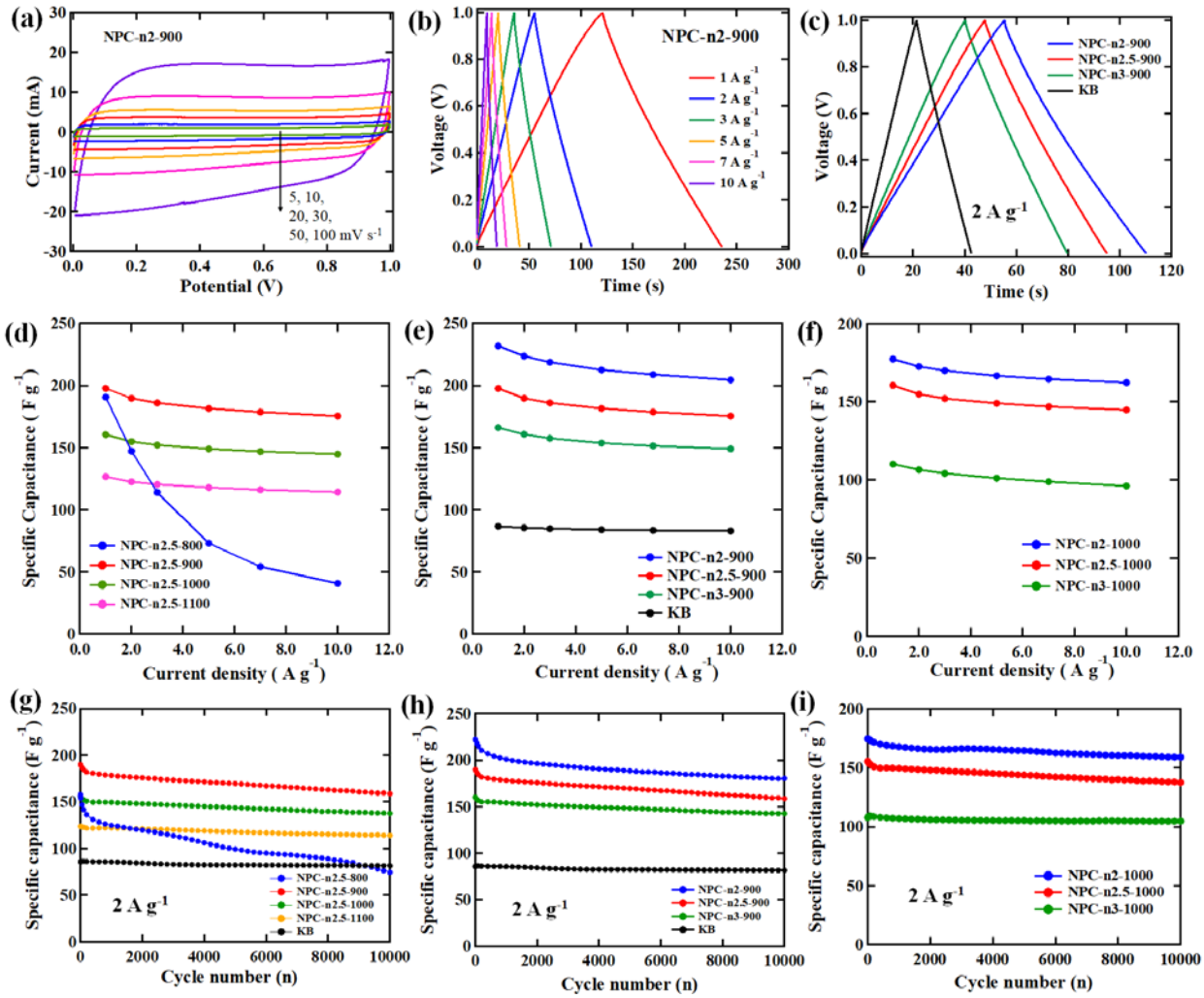
Figure 9. Electrochemical performance of NPCs in two-electrode supercapacitor measurements. (a) The typical CV curves at different scanning rates; (b, c) the typical charge-discharge curves; (d, e, f) capacitance at different current densities; (g, h, i) cycling performance.